

Linear electro-optic effect in multiferroic BiFeO₃ thin filmsD. Sando,^{1,2} P. Hermet,³ J. Allibe,¹ J. Bourderionnet,⁴ S. Fusil,¹ C. Carrétéro,¹ E. Jacquet,¹ J.-C. Mage,¹ D. Dolfi,⁴ A. Barthélémy,¹ Ph. Ghosez,³ and M. Bibes^{1,*}¹*Unité Mixte de Physique CNRS/Thales, 1 Avenue Fresnel, Campus de l'Ecole Polytechnique, 91767 Palaiseau, France and Université Paris-Sud, 91405 Orsay, France*²*Center for Correlated Electron Systems, Institute for Basic Science (IBS), and Department of Physics and Astronomy, Seoul National University, 1 Gwanak-ro, Gwanak-gu, Seoul 151-747, Republic of Korea*³*Physique Théorique des Matériaux, Université de Liège, B-4000 Sart Tilman, Belgium*⁴*Thales Research and Technology France, 1 Avenue Fresnel, Campus de l'Ecole Polytechnique, 91767 Palaiseau, France*
(Received 18 April 2013; revised manuscript received 7 April 2014; published 7 May 2014)

Multiferroics are materials with coexisting magnetic and ferroelectric orders, which show potential for electrically controlled spintronic devices. A common application of ferroelectrics is in electro-optical modulators exploiting their electric-field-dependent optical indices. The coupling of optical and magnetic degrees of freedom is attractive for designing multifunctional devices, but to date the electro-optical response of multiferroics has hardly been explored. Here we report a joint experimental and theoretical study of this effect in multiferroic BiFeO₃ thin films. We confirm the large birefringence present in single crystals and determine the electro-optic coefficients r_{13} and r_{33} . We present approaches to increase the obtained coefficients, for instance, by using tetragonal-like BiFeO₃, and expand the potential of multiferroics to optical applications.

DOI: [10.1103/PhysRevB.89.195106](https://doi.org/10.1103/PhysRevB.89.195106)

PACS number(s): 77.55.Nv, 71.15.Mb, 78.20.Jq

I. INTRODUCTION

BiFeO₃ (BFO) has captured the attention of a great number of research groups in recent years on account of its room-temperature multiferroic properties [1]. Multiferroism refers to the existence of multiple ferroic orders [2] and the coupling of these orders can lead to exciting application opportunities [3]. For instance, the coupling of the antiferromagnetic and ferroelectric orders in BFO can be used to control the magnetic state via an electric field [4,5]. This functionality finds interest in spintronics and memory applications. Other important properties of BFO are its remarkable spontaneous polarization of 100 $\mu\text{C}/\text{cm}^2$ in the $\langle 111 \rangle$ pseudocubic direction [6], its high Curie temperature of 1100 K [1], and its tunable magnetic order [7] and spin excitations [8]. In addition to its robust ferroelectricity and rich spin physics, BFO exhibits interesting optical characteristics such as a band gap in the visible range (2.7 eV), a large birefringence [9], and weak absorption at 1.55 μm [10], a wavelength that is relevant for technological applications.

The electro-optic modulator (EOM) is a well-established device that is indispensable in the telecommunications industry. Standard EOMs are macroscopic components based on single crystals of ferroelectric lithium niobate (LiNbO₃). Recently, however, there has been an effort to create thin-film EOMs with ferroelectric BaTiO₃ (BTO) as the modulating medium [11]. One complication with BTO, however, is its ferroelectric transition just above room temperature, which can cause instabilities for modulators operating over wide temperature ranges. BFO, on the other hand, with its ferroelectric transition temperature much higher than ambient, may therefore offer promise for compact thin-film EOMs operating over a wide temperature range.

An important characteristic of materials used in EOMs is the electro-optic (EO) tensor. The tensor elements give a

measure of how efficiently an electrical signal can be converted to an optical signal and thus form an important metric for the applications potential of a material. Although some optical properties of BFO have now been investigated [10,12,13], the EO coefficients of this medium have not yet been elucidated. The knowledge of these properties is an important step for the potential integration of BFO into high-bandwidth compact EOM devices [11]. To that end, here we report measurements of the EO coefficients of BFO and compare the measured results with the findings of first-principles calculations.

The linear EO tensor describes the change of a medium's optical refractive index induced at linear order by a static or low-frequency field (the Pockels effect) through

$$\Delta \left(\frac{1}{n^2} \right)_{ij} = \sum_{\gamma=1}^3 r_{ij\gamma} E_{\gamma}, \quad (1)$$

where the summation runs over the spatial directions γ ($1 = x$, $2 = y$, and $3 = z$). In the point group $3m$, the EO tensor has four independent elements (see the Appendix): r_{11} , r_{51} , r_{13} , and r_{33} , using Voigt notation for the first two indices. In most applications the applied field is $\mathbf{E} = (0, 0, E)$. For *birefringent* materials with $3m$ symmetry, such as BFO and lithium niobate (LiNbO₃), $n_x = n_y = n_o$ and $n_z = n_e$, where n_o and n_e are the ordinary and extraordinary refractive indices of the medium, respectively, and the modulation simplifies, at linear order, to

$$n_o(E) = n_o - \frac{1}{2} r_{13} n_o^3 E, \quad n_e(E) = n_e - \frac{1}{2} r_{33} n_e^3 E. \quad (2)$$

It is usual to define an effective electro-optic coefficient as $r_{\text{eff}} = r_{33} - r_{13}(n_o^3/n_e^3)$. There are various methods for measuring the values of r_{eff} . In the present work, we combine both a reflection method [14,15] and a transmission method [15,16]. They require single-domain films of BFO, in specific orientations; in the following we describe our experimental approaches for achieving this.

*manuel.bibes@thalesgroup.com

II. THIN-FILM GROWTH, FERROELECTRIC, AND OPTICAL CHARACTERIZATION

To measure the r coefficients of BFO using the reflection method, films of 5%-Mn-doped BFO ~ 525 nm thick were grown on (111)-oriented SrTiO₃ (STO) substrates by pulsed laser deposition [17] with 20-nm-thick semitransparent SrRuO₃ (SRO) bottom electrodes. Mn doping was used to reduce leakage [18]. High-angle x-ray-diffraction spectra, measured using a Bruker D8 system, indicate single-phase epitaxial growth of BFO, as shown in Figs. 1(a) and 1(b). Atomic force microscopy topography images (not shown) indicate an average film roughness of 1–2 nm. Next, gold top electrodes ($100 \times 100 \mu\text{m}^2$ and $30 \times 30 \mu\text{m}^2$ in size) were deposited using dc sputtering through a shadow mask. The poling process of the BFO is demonstrated using piezoresponse force microscopy (PFM); see out-of-plane amplitude images in Fig. 1(f). We placed the tip in contact with the top electrode and applied a tip bias to pole the BFO under the electrode in the [111] direction. After poling, the (111) BFO film is monodomain with no measurable in-plane piezoresponse; i.e. BFO is single variant with ferroelectric polarization, and thus the optic axis, perpendicular to the film surface. To illustrate successful ferroelectric switching, we performed polarization hysteresis loops, measured on the $100 \times 100 \mu\text{m}^2$ electrodes using an Aixact TF2000, at 400 Hz. An example of such hysteresis loops, presented in Fig. 2(f), shows a remanent polarization of $\sim 100 \mu\text{C}/\text{cm}^2$.

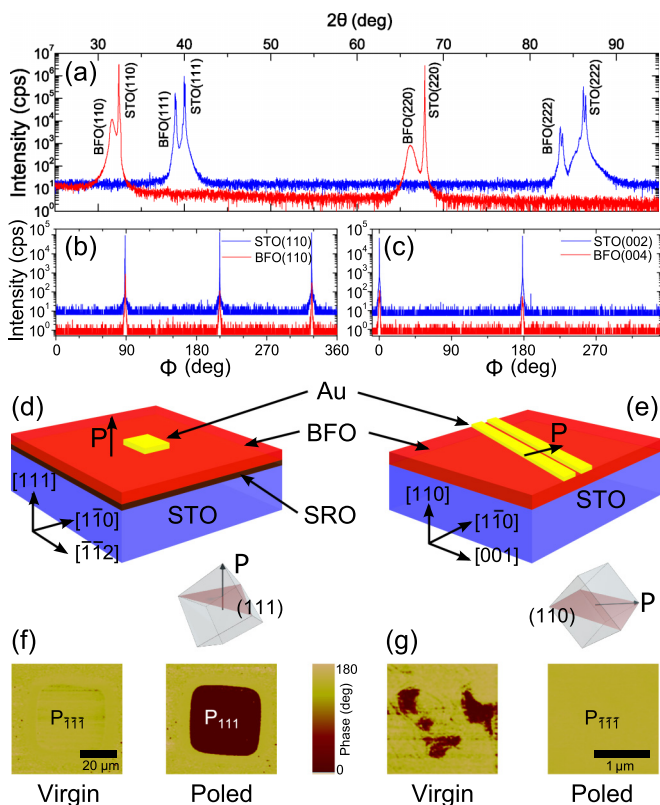


FIG. 1. (Color online) (a) Scans of 2θ - ω and ϕ for the (b) reflection and (c) transmission samples, illustration of the (d) reflection and (e) transmission samples, (f) out-of-plane PFM images through top electrodes of the reflection sample, and (g) in-plane phase PFM images between the electrodes for the transmission sample.

For measurements in the transmission geometry, ~ 460 -nm-thick 5%-Mn-doped BFO films were grown on STO (110). X-ray diffraction indicates single-phase epitaxial growth [Figs. 1(a) and 1(c)]. Planar electrodes of gold, spaced by $5 \mu\text{m}$ and aligned perpendicular to the [111] direction, were deposited by sputtering and lift-off. In-plane PFM [Fig. 1(g)] shows that the sample was almost a monodomain as grown. We applied 350 V across the planar electrodes to fully pole the BFO. After poling, the PFM in-plane phase was uniform [Fig. 1(g)] with maximum amplitude when the cantilever was parallel to the electrodes, while no out-of-plane amplitude was measured. This indicated that the ferroelectric polarization was perpendicular to the electrodes, i.e., single variant along the in-plane [111] direction.

The optical properties of the reflection and transmission samples were measured by spectroscopic ellipsometry, over a spectral range of 300–2000 nm [12]. The ellipsometry measurements allowed us to confirm the thickness of the films and determine the complex refractive index of the BFO and SRO layers. A multilayer model, where the BFO layer was described by three Tauc-Lorentz oscillators, was formulated. Through fitting the model to the data, the BFO dispersion law was extracted. In the case of the transmission sample, since the BFO film is almost single-domain with the optic axis in the plane of the film, using ellipsometry we can extract the two refractive indices n_o and n_e [19]. Due to the strong birefringence of BFO [9], a rotation about the sample normal means that the ellipsometry measurement probes varying proportions of the ordinary and extraordinary refractive indices n_o and n_e . In Fig. 2(b) the real part of the refractive index at 1550 nm is plotted against the azimuthal rotation angle ϕ . Fitting these data to the theory based on an ellipsometry incident angle of 70° yields the values of n_o and n_e . This analysis allows us to determine the dispersion law for n_o and n_e separately [Fig. 2(d)] and the birefringence of BFO over a broad wavelength range [Fig. 2(e)]. The maximum value of birefringence is about 0.27, which is slightly smaller than the 0.34 reported at 550 nm in single crystals [9]. The difference observed here could be due to the imperfect ferroelectric polarization state in our film. This birefringence is, however, still very high compared to other ferroelectrics such as BaTiO₃ (0.05) [20] and LiNbO₃ (0.09) [21].

The optical properties of the bottom electrode SRO were also determined by spectroscopic ellipsometry over the (300–2000)-nm range. A three-layer model was formulated based on four Tauc-Lorentz oscillators [22] and fitting the model to the data yielded the dispersion law for SRO, shown in Fig. 2(c). The resulting dispersion law allowed accurate determination of the effect of the SRO layer on the optical measurements, as we describe later.

III. MEASUREMENT OF ELECTRO-OPTIC COEFFICIENTS

The Teng-Man technique [14,15] is a routine method for determining EO coefficients in a reflection geometry. As illustrated in Fig. 3(a), a laser beam (with polarization at 45°) is focused through the substrate and thin film (with its ferroelectric polarization perpendicular to the film plane) at an incidence angle of 45° onto the top electrode, from which

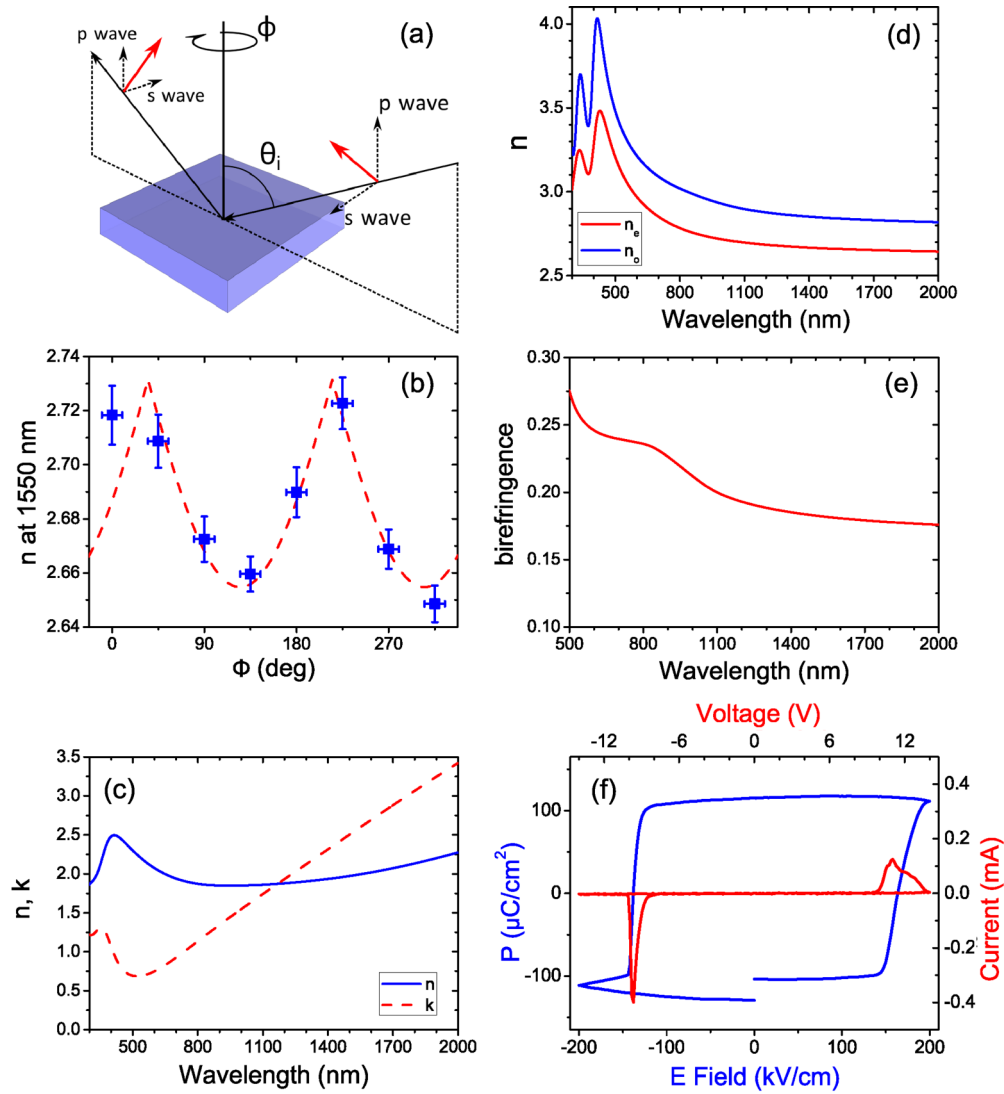


FIG. 2. (Color online) Optical and ferroelectric properties of the samples: (a) ellipsometry setup with angles indicated, (b) dependence of the measured BFO index on sample angle in the ellipsometry measurement, (c) dispersion law of SrRuO₃, (d) ordinary and extraordinary refractive indices of BFO, (e) birefringence of BFO thin film, and (f) polarization hysteresis loop of BFO on the (111)-oriented sample.

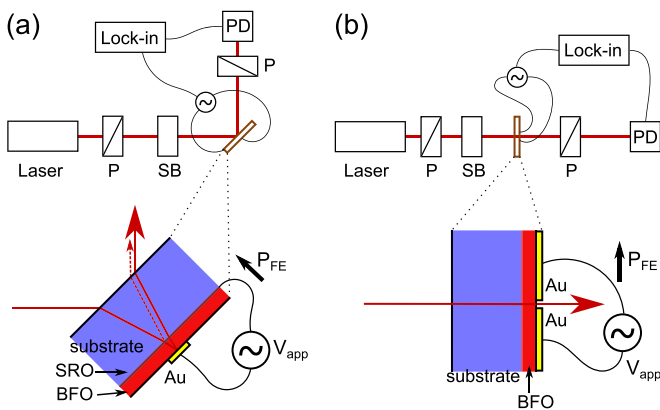


FIG. 3. (Color online) Experimental layout for (a) reflection and (b) transmission measurement of EO coefficients: P, polarizer; SB, Soleil-Babinet compensator; PD, photodiode; and Lock-in, lock-in amplifier.

it reflects and propagates back through the sample. An ac electric field E_{elec} is then applied between the electrodes to modify the refractive index of the medium for the s and p components of polarization of the beam according to (2). The induced path-length difference between the two components results in a phase shift between them upon exit of the medium. An analyzer converts this phase shift into an intensity modulation, which is measured by a photodiode locked to the frequency of the excitation voltage.

Alternatively, one may use a transmission technique [15,16]; here the ferroelectric material is poled in the film plane and the laser beam passes through the slit of two planar electrodes [see Fig. 3(b)]. As in the reflection method, the input beam is polarized at 45° and an ac voltage applied to the electrodes induces a modulation in the beam, which is again detected using a lock-in technique. In our experiments, for both geometries, a 4-mW fiber diode laser at 1.55 μm was used. For reflection (transmission) measurements, microscope objectives were used to focus the beam onto the 100-μm

gold pads (through the 5- μm stripe between electrodes) and to expand the beam for projection onto the photodiode. A Soleil-Babinet compensator (SBC) was used to modify the phase difference between the s and p components of the beam.

For both methods, the reflected (transmitted) optical field, after passing through the crossed analyzer (see Fig. 3), reads

$$\begin{aligned} E_{\text{out}} &= \frac{1}{2} \begin{pmatrix} 1 & -1 \\ -1 & 1 \end{pmatrix} \times \begin{pmatrix} \kappa_s & 0 \\ 0 & \kappa_p \end{pmatrix} \\ &\times \begin{pmatrix} e^{i\varphi_{\text{SBC}}} & 0 \\ 0 & 1 \end{pmatrix} \times \frac{E_0}{\sqrt{2}} \begin{pmatrix} 1 \\ 1 \end{pmatrix} \\ &= \frac{E_0}{2\sqrt{2}} (\kappa_s e^{i\varphi_{\text{SBC}}} - \kappa_p) \begin{pmatrix} 1 \\ 1 \end{pmatrix}, \end{aligned} \quad (3)$$

where κ_s and κ_p are the reflection (transmission) coefficients of the samples for s and p waves, respectively; φ_{SBC} is the phase shift between s and p waves, imparted by the SBC; and E_0 is the electric-field amplitude of the incident beam. The dc voltage generated by the photodiode is then given by

$$V_{\text{dc}} = \rho_{\text{PD}} \eta \frac{E_0^2}{2} [\tau_s^2 + \tau_p^2 - 2\tau_s \tau_p \cos(\varphi_{\text{SBC}} + \varphi_s - \varphi_p)], \quad (4)$$

where $\tau_{s,p}$ and $\varphi_{s,p}$ respectively stand for the modulus and argument of $\kappa_{s,p}$. The photodiode load and efficiency are given by ρ_{PD} and η , respectively. When E_{elec} (of amplitude m) is applied to the film, the corresponding voltage modulation V_{sync} detected by the lock-in amplifier is given by

$$\begin{aligned} V_{\text{sync}} &= m \times \frac{\partial V_{\text{dc}}}{\partial E_{\text{elec}}} \\ &= m \rho_{\text{PD}} \eta \frac{E_0^2}{2} \left(\frac{\partial(\tau_s^2 + \tau_p^2)}{\partial E_{\text{elec}}} \right. \\ &\quad - 2 \frac{\partial(\tau_s \tau_p)}{\partial E_{\text{elec}}} \cos(\varphi_{\text{SBC}} + \varphi_s - \varphi_p) \\ &\quad \left. + 2\tau_s \tau_p \frac{\partial(\varphi_s - \varphi_p)}{\partial E_{\text{elec}}} \sin(\varphi_{\text{SBC}} + \varphi_s - \varphi_p) \right). \end{aligned} \quad (5)$$

We have derived numerical multilayer models for the reflection (transmission) sample using the 4×4 matrix formulation method introduced by Yeh [23], using the experimental layer thicknesses and refractive indices, given in Table I. The reflection (transmission) coefficients κ_s and κ_p and their derivatives with respect to the applied electric field, these being functions of the EO coefficients r_{13} and r_{33} , were calculated.

The experimental procedure first consists of collecting the optical bias curve (OBC) [25], that is, plotting the dc photodiode signal V_{dc} when the SBC is scanned through its range and no ac voltage is applied to the film. With $\tau_{s,p}$ and

$\varphi_{s,p}$ known from the numerical model, the adjustment of the OBC with Eq. (4) gives the scaling coefficient $\rho_{\text{PD}} \eta E_0^2$ and allows the SBC calibration with φ_{SBC} as a function of the SBC position [see Figs. 4(a) and 4(b)].

Next the ac excitation voltage is applied to the film and the dependence V_{sync} of the lock-in signal on the SBC position is recorded. First, the measurements presented in Figs. 4(a) and 4(b) show that the transmission and reflection samples behave differently, with a V_{sync} curve close to the OBC derivative in the transmission case, while the V_{sync} and OBC curves are almost in phase in the reflection case. In order to understand from where this difference arises, simplified analytical expressions can be derived for the coefficients κ , referred to as r and t for reflection and transmission samples, respectively. In both cases, multiple interferences are only considered in the BFO layer. For the simplest case of the transmission sample, we have

$$t \cong K_t \left(\frac{e^{i\psi}}{1 - r_{\text{BFO/STO}} r_{\text{BFO/air}} e^{2i\psi}} \right) \cong K_t e^{i\psi}, \quad (6)$$

with $K_t = t_{\text{air/STO}} \times t_{\text{STO/BFO}} \times t_{\text{BFO/air}}$. The phase term ψ corresponds to the propagation along the thickness of the BFO layer. In this case, since K_t is real, the $\varphi_{s,p}$ terms to substitute into Eq. (5) are directly given by ψ , formulated for s and p waves. Their derivatives with respect to the applied electric field are given by

$$\frac{\partial(\varphi_s - \varphi_p)}{\partial E} = \frac{\pi}{\lambda} n_e^3 (r_{33} - r_{13} n_o^3 / n_e^3) L_{\text{BFO}}, \quad (7)$$

with L_{BFO} the thickness of the BFO layer and n_o and n_e the ordinary and extraordinary indices of BFO. With $\partial K_D / \partial E \ll \partial \phi / \partial E$, the cosine term in Eq. (5) is negligible, which makes the V_{sync} term behave like the derivative of the OBC. It also follows from Eq. (7) that the transmission method is only sensitive to $r_{\text{eff}} = r_{33} - r_{13} n_o^3 / n_e^3$ and does not allow the independent determination of the two coefficients.

For the reflection sample, assuming a reflection coefficient of -1 for the BFO/gold interface, the reflection coefficient can be approximated by

$$r = K_r \left(r_{\text{SRO/BFO}} - \frac{t_{\text{SRO/BFO}} t_{\text{BFO/SRO}} e^{2i\psi}}{1 + r_{\text{BFO/SRO}} e^{2i\psi}} \right), \quad (8)$$

which can be simplified to

$$r = K_r \left(\frac{r_{\text{SRO/BFO}} - e^{2i\psi}}{1 - r_{\text{SRO/BFO}} e^{2i\psi}} \right), \quad (9)$$

with $K_r = t_{\text{air/STO}} \times t_{\text{STO/SRO}} \times t_{\text{STO/SRO}} \times t_{\text{SRO/STO}}$. The important thing here is that the SRO is a conductive oxide, with a complex refractive index. If SRO had a real refractive index, then from Eq. (9) we would have $|r| = |K_r|$ and Eq. (7) would

TABLE I. Thicknesses and optical indices, at 1550 nm, for the various layers.

Material	Thickness (nm)	n_o	n_e	k	Source
SRO	20 ± 5	1.995		2.6003	ellipsometry
BFO reflection	525 ± 15	2.79 ± 0.03	2.65 ± 0.03	0	ellipsometry
BFO transmission	460 ± 10	2.79 ± 0.03	2.65 ± 0.03	0	ellipsometry
gold	50 ± 5	0.53		10.79	[24]

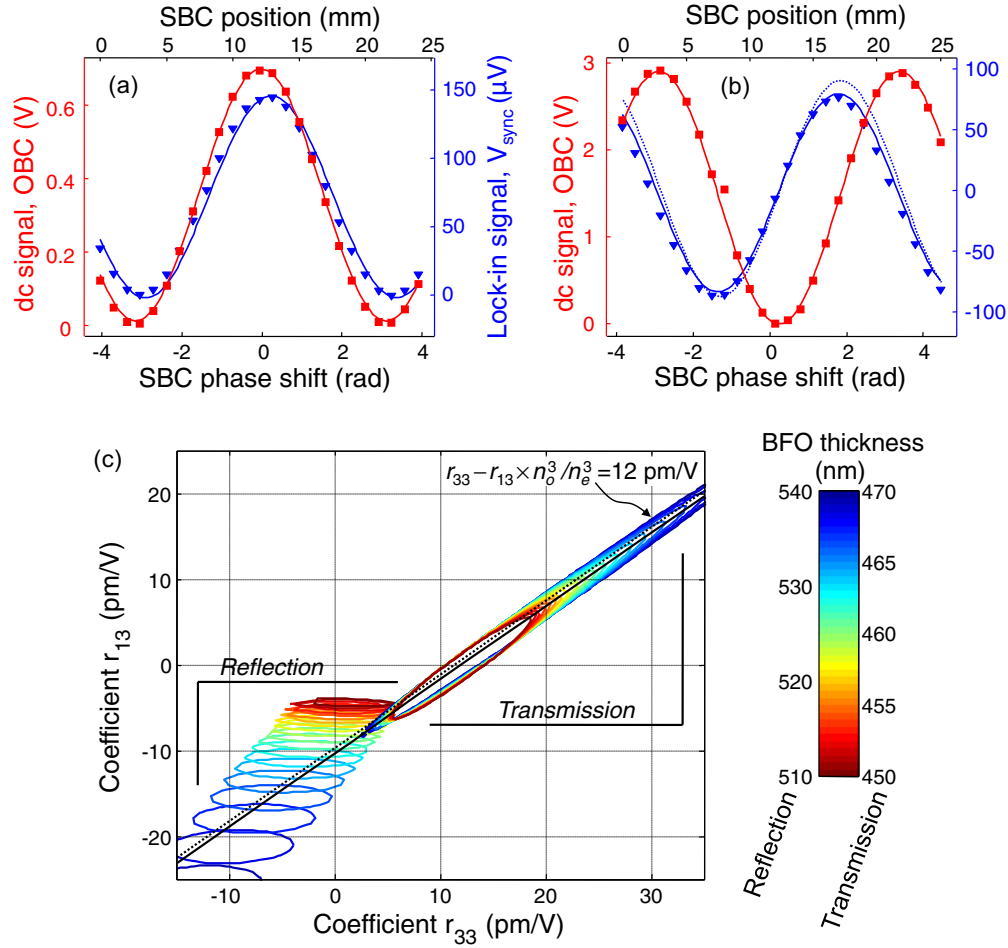


FIG. 4. (Color online) Optical bias curve V_{OBC} and modulation curve V_{sync} for (a) reflection and (b) transmission samples. Symbols are experimental measurements and lines are theoretical fits with $r_{13} = -6.4 \text{ pm/V}$ and $r_{33} = 4.4 \text{ pm/V}$ for the reflection sample with a BFO thickness of 520 nm and the transmission sample with a BFO thickness of 460 nm. Solid lines correspond to the rigorous multilayer model, while the dotted lines are for simplified expressions. (c) Measurement analysis of reflection and transmission samples. Circled (r_{13}, r_{33}) regions correspond to an error between measured and calculated V_{sync} of less than 0.6%. The color scale indicates the BFO layer thickness range for both samples.

apply, with, as for the transmission case, an OBC derivativelike behavior of the V_{sync} curve. Essentially, the fact that n_{SRO} is complex causes $|r|$ to depend on ψ , which increases its derivative with respect to the applied field. To some extent, this balances the weights of the sine and cosine terms in Eq. (5), which qualitatively explains the phase shift of the experimental measurements for the reflection sample compared with the transmission curves.

From Eqs. (5)–(7), for the transmission sample we can derive an approximate expression for r_{eff} as a function of the amplitudes V_{OBC}^0 and V_{sync} of the OBC and the lock-in signal curves, respectively, the amplitude m of the applied electric field, and the thickness L_{BFO} of the BFO layer:

$$r_{\text{eff}} = r_{33} - r_{13} n_o^3 / n_e^3 = \frac{V_{\text{sync}}^0}{m V_{\text{OBC}}^0} \frac{\lambda}{\pi n_e^3 L_{\text{BFO}}}. \quad (10)$$

With a BFO thickness of $460 \pm 10 \text{ nm}$, we obtain the approximate value $r_{\text{eff}} = 12.0 \pm 0.3 \text{ pm/V}$, plotted as the dotted line in Fig. 4(c). To extract r_{13} and r_{33} from our measurements and our rigorous multilayer model, we calculated V_{sync} over

an estimated range of r_{13} and r_{33} values and over the thickness range of the BFO layer defined by the measurement uncertainty reported in Table I. An error estimator ϵ is defined by

$$\epsilon = \frac{1}{N_{\text{SBC}} V_{\text{sync}}^0} \sqrt{\sum_{\text{SBC positions}} |V_{\text{sync,calc}} - V_{\text{sync}}|^2}, \quad (11)$$

where N_{SBC} is the number of experimental positions of the SBC. In Fig. 4(c) the (r_{13}, r_{33}) regions defined by $\epsilon \leq 0.6\%$ are circled for both reflection and transmission samples and over their respective thickness ranges (indicated by the color scales). For the transmission sample, the rigorous model yields $r_{\text{eff}} = 10.9 \pm 1.1 \text{ pm/V}$, consistent with the approximate result obtained from (10). For the reflection sample, given a precision of $\pm 15 \text{ nm}$ for the BFO thickness, we obtain $r_{33} = 4.4 \pm 1.3 \text{ pm/V}$ and $r_{13} = -6.4 \pm 2.0 \text{ pm/V}$.

IV. FIRST-PRINCIPLES CALCULATIONS

To gain further insight into our experimental measurements, we have performed first-principles calculations. Calculations

of the $R3c$ [26] and Cm bulk phases of BiFeO_3 were performed within density functional theory (DFT) and the local spin-density approximation (LSDA) as implemented in the ABINIT package [27]. An antiferromagnetic (AFM) structure was imposed for both phases (G type for the $R3c$ phase and C type for the Cm phase). We used plane waves and optimized pseudopotentials [28]. Bismuth ($5d$, $6s$, and $6p$), iron ($3s$, $3p$, $3d$, and $4s$), and oxygen ($2s$ and $2p$) electrons were considered as valence states. Convergence was reached for a 57-hartree plane-wave kinetic-energy cutoff and a $6 \times 6 \times 6$ mesh of special k points. The atomic positions and lattice parameters were relaxed until the maximum residual forces on the atoms were less than 5×10^{-6} hartree bohr $^{-1}$ and the stresses less than 6×10^{-8} hartree bohr $^{-3}$. Dynamical matrix, dielectric constants, and Born effective charge Z^* tensors were computed within a variational approach to density-functional perturbation theory [29]. The Raman susceptibility tensors were obtained within a nonlinear response formalism, making use of the $2n + 1$ theorem [30].

The clamped EO coefficients $r_{ij\gamma}$ can be conveniently decomposed into a purely electronic contribution and a phonon-mediated response that, in the case of uniaxial crystals, can be written (in cgs units) as [31]

$$r_{ij\gamma} = \frac{-8\pi}{n_i^2 n_j^2} \chi_{ijl}^{(2)} \Big|_{l=\gamma} - \frac{4\pi}{n_i^2 n_j^2 \sqrt{\Omega}} \sum_m \frac{\alpha_{ij}^m p_{m,\gamma}}{\omega_m^2}, \quad (12)$$

where n_i and n_j are the refractive indices, $\chi^{(2)}$ are the nonlinear optical susceptibilities, m runs over the transverse-optical (TO) modes, ω_m are the TO mode frequencies, p_m are the TO mode polarities (linked to the IR intensities through $S_{m,\alpha\beta} = p_{m,\alpha} p_{m,\beta}$), α^m are the TO mode Raman susceptibilities, and Ω is the unit cell volume. The EO coefficients and relevant quantities in (12) were computed following the linear-response scheme described in Ref. [32]. These clamped coefficients do not include any possible strain relaxation in the quasistatic field.

A. The $R3c$ phase

We first consider the $R3c$ phase of BFO in order to make a comparison with the present experimental results. For the relaxed atomic structure, phonon frequencies, and IR and Raman intensities (see the Appendix) we have recovered the results previously published in Ref. [26]. The linear and nonlinear optical susceptibilities are reported in Table II. In order to empirically correct for a well-known limitation of the LSDA, we used a scissors correction of 2 eV that adjusts the electronic band gap to a value of 2.8 eV [33]. With this correction, the refractive indices only slightly overestimate the experimental values of Table I. The nonlinear susceptibilities appear to be strongly sensitive to the scissors correction and also differ significantly from a previous calculation that nevertheless neglected local-field corrections [33]. Unfortunately, no reliable experimental data are available for $\chi^{(2)}$, the only recent measurements by Kumar *et al.* [10] having been taken close to a resonant frequency.

The computed clamped EO coefficients are reported in Table III, together with their individual electronic and mode-by-mode phonon-mediated contributions. The r_{13} and r_{33}

TABLE II. Calculated refractive indices and nonlinear optical susceptibilities of bulk BFO in the $R3c$ phase (using Voigt notation for the first two indices, $d_{ij} = 1/2\chi_{ij}^{(2)}$, in pm/V), obtained within the LSDA and with an additional scissors correction of 2 eV (LSDA + SCI). Our results are compared to a previous calculation in generalized gradient approximation plus Hubbard U (GGA+ U) ($U = 7$ eV and $J = 0.9$ eV) with an independent-particle approximation (neglecting local-field corrections) [33].

Parameter	LSDA ^a	LSDA + SCI ^a	GGA+ U ^b
n_o	3.89	2.99	2.65
n_e	3.55	2.79	2.55
d_{11}	-125.63	-19.20	6.49
d_{15}	60.95	8.39	-3.54
d_{33}	32.12	-2.11	-3.94

^aPresent work.

^bReference [33].

coefficients are linked to the A_1 modes, polarized along the optical axis, while the r_{11} and r_{51} coefficients are linked to the E modes, polarized perpendicular to it. First, we notice that the electronic contribution is typically small and of the order of 1 pm/V, rather independently of the uncertainty related to the scissors correction. Then the r_{33} and r_{51} coefficients exhibit significant ionic contributions that come from the $A_1(\text{TO3})$ and $E(\text{TO5})$ modes, respectively. The lattice response makes r_{33} and r_{51} significantly large, but they remain nevertheless smaller than in compounds such as LiNbO_3 [31]. The smaller amplitude of the computed r_{13} with respect to r_{33} comes from the smaller contribution of the $A_1(\text{TO3})$ mode and is related to the strong anisotropy of its Raman tensor [$a = -0.0061$ bohr $^{3/2}$ and $b = -0.0406$ bohr $^{3/2}$ (see Table IV in the Appendix)]. We notice that replacing the computed frequencies by the experimental frequencies of Ref. [34] in (12) only marginally changes the values of r_{13} and r_{33} (by less than 0.5 pm/V). The amplitude of the lattice contribution is much more sensitive to the scissors correction. In the present calculation, this arises from the renormalization of the refractive indices that globally appear at the fourth power in (12). In this context, the scissors-corrected values should be closer to the experiment. Making use of the experimental refractive indices ($n_o = 2.79$ and $n_e = 2.65$) in (12) provides the following estimates: $r_{13} = 3.16$ pm/V, $r_{33} = 14.75$ pm/V, and $r_{\text{eff}} = 11.06$ pm/V.

Our calculations thus nicely reproduce the measured value of r_{eff} but do not agree with the individual values extracted for r_{33} and r_{13} . On the one hand, our calculations strongly overestimate the value of r_{33} . On the other hand, they do not support the opposite sign and larger amplitude of r_{13} . Calculating EO coefficients remains challenging at the DFT level, although it has previously provided a good qualitative description in this class of compounds [31]. We point out that the calculations are restricted to the *clamped* EO coefficients. They were also performed at the bulk level and so neglect the effect of the epitaxial mechanical constraints imposed experimentally on the thin films. Furthermore, our Raman tensors were computed without the scissors correction. Although this is common practice, the agreement between theoretical and experimental Raman spectra is not quantitatively perfect in

TABLE III. Calculated electronic and ionic contributions to the electro-optic tensor (in pm/V) of the $R3c$ phase of BiFeO_3 . The ionic part is split into individual contributions of distinct TO modes. Frequencies ω_m are in cm^{-1} . Our results make use of scissors correction for the refractive indices and nonlinear optical susceptibilities (LSDA + SCI values in Table II). Values calculated without scissors correction are also shown in parentheses for comparison.

Calculated contribution	E modes			A_1 modes			
	ω_m	r_{11}	r_{51}	ω_m	r_{13}	r_{33}	
electronic		(2.20) 0.96	(-1.28) -0.48		(-1.07) -0.42	(-0.81) 0.14	
ionic	TO1	102	(-0.34) -0.97	(0.28) 0.76	167	(0.62) 1.77	(0.50) 1.31
	TO2	152	(1.18) 3.39	(-0.71) -1.94	266	(-0.05) -0.14	(0.19) 0.49
	TO3	237	(0.01) 0.02	(0.26) 0.72	320	(0.36) 1.03	(3.46) 9.07
	TO4	263	(0.29) 0.83	(0.19) 0.53	517	(0.06) 0.16	(0.38) 1.00
	TO5	275	(-0.46) -1.33	(3.86) 10.59			
	TO6	335	(-0.05) -0.15	(-0.16) -0.45			
	TO7	378	(-0.04) -0.11	(0.01) 0.03			
	TO8	408	(0.03) 0.08	(-0.12) -0.32			
	TO9	509	(0.20) 0.58	(0.098) 0.27			
	sum of ionic		(0.82) 2.34	(3.72) 10.20		(0.98) 2.82	(4.53) 11.87
total			(3.02) 3.31	(2.44) 9.71		(-0.08) 2.40	(3.72) 12.00

the case of BiFeO_3 [26]. There are, however, no experimental data available in the literature to which we can compare our computed Raman tensors.¹

Typically, in ferroelectrics, a pronounced EO response arises from a large ionic contribution that, as understandable from (12), is linked to a low-frequency mode combining high polarity and high Raman intensity [31]. In $R3c$ BFO, the most polar $A_1(\text{TO3})$ and $E(\text{TO5})$ modes are also those with the largest Raman intensity (see Table I of Ref. [26]), but they are at a rather high frequency. The softening of these modes through epitaxial strain engineering might be a way to enlarge the EO response. Playing with substrate orientation and epitaxial strain to stabilize BFO in another phase with distinct dynamical properties is another (and likely more promising) way to achieve a large EO response.

B. The Cm phase

We have carried out a similar DFT study of a so-called $Cm-C$ phase of BFO that was recently proposed [36] as a plausible supertetragonal phase for BFO films epitaxially grown on a (001)- LaAlO_3 substrate [37,38]. The calculations were performed in a fully relaxed (i.e., not including any mechanical constraint) primitive ten-atom Cm phase with C -type AFM structure.

The complete set of results is provided in the Appendix. In order to allow a more direct comparison with what would be observed experimentally, we moved from the primitive ten-atom cell to a 40-atom cell in which the z axis is nearly aligned with the long \mathbf{c}_{II} axis. This axis corresponds to the expected growth direction for a $Cm-C$ BFO film grown on a

(001) substrate and is also the direction along which an electric field can be conveniently applied in practical experiments. Within this system of coordinates (see the Appendix), the different tensors of the *bulk* $Cm-C$ phase (i.e., neglecting epitaxial constraints that will additionally appear in thin films) are written

$$\epsilon_{ij}^{\infty} = \begin{pmatrix} 8.37 & 0.00 & 0.00 \\ 0.00 & 6.04 & -0.12 \\ 0.00 & -0.12 & 6.93 \end{pmatrix}, \quad (13)$$

$$d_{ij} = \begin{pmatrix} 0.00 & 0.00 & 0.00 & 0.00 & 37.88 & 17.70 \\ 17.70 & -9.73 & -13.92 & -8.89 & 0.00 & 0.00 \\ 37.88 & -8.89 & 6.83 & -13.92 & 0.00 & 0.00 \end{pmatrix}, \quad (14)$$

$$r_{i\gamma} = \begin{pmatrix} 0.00 & -6.07 & 59.60 \\ 0.00 & 17.77 & -12.22 \\ 0.00 & -6.56 & 22.04 \\ 0.00 & -1.11 & -1.07 \\ 18.07 & 0.00 & 0.00 \\ 20.84 & 0.00 & 0.00 \end{pmatrix}. \quad (15)$$

Our DFT calculations for the supertetragonal $Cm-C$ phase of BFO thus predict that some clamped EO coefficients may be as large as 60 pm/V, i.e., 5 times larger than in the $R3c$ phase, and even much larger than those computed for LiNbO_3 [31]. With this knowledge, it may be that this tetragonal-like (T -like) BFO will hold more promise in electro-optical applications. Interestingly, this polymorph of BFO shows a multiferroic phase transition just above 300 K [39,40] near which an enhancement of the EO response could occur [32].

V. SUMMARY

In this paper we have reported the birefringence and the two most important linear electro-optic coefficients r_{13} and r_{33} of epitaxial BiFeO_3 thin films. Using spectroscopic ellipsometry measurements, we confirmed that the large birefringence

¹A recent experimental estimate of the a and b Raman coefficients of the $A_1(\text{LO3})$ mode suggests that they might instead be close in amplitude and opposite in sign [35]. However, the experiment was in a resonant configuration: It was carried out at room temperature with an excitation source at 532 nm. This corresponds to an energy of 2.33 eV, which is very close to the expected BFO band gap at 300 K.

present in single crystals indeed exists for thin films. Through detailed experimental measurements on (111)- and (110)-oriented epitaxial BFO films on STO substrates, we found the effective electro-optic coefficient $r_{\text{eff}} = 12.0 \pm 0.3$ pm/V, with $r_{33} = 4.4$ pm/V and $r_{13} = -6.4$ pm/V. Our DFT calculations successfully reproduced the measured value of r_{eff} , but not the individual values of r_{13} and r_{33} . While the $R3c$ phase of BFO appears to produce sizable but not exceptionally large EO coefficients, our calculations indicate that the Cm - C phase should produce a stronger response. We hope that this work will encourage further experimental characterization of the optical properties of the R phase and verification of the predicted improved EO response in the T -like phase of BFO.

ACKNOWLEDGMENTS

We acknowledge financial support from the French Agence Nationale de la Recherche through projects Meloïc, Nomilops, and Multidolls. Ph.G. acknowledges a Research Professorship from the Francqui Foundation and financial support from the ARC project TheMoTherm. We thank S. Trolhier-McKinstry for useful comments.

APPENDIX: FIRST-PRINCIPLES CHARACTERIZATION OF THE $R3c$ AND Cm PHASES OF BiFeO_3

1. The $R3c$ phase

Calculations were performed in the primitive ten-atom $R3c$ phase with G -type AFM structure, considering Cartesian coordinates with the z axis aligned along the polar axis, i.e., the [111] pseudocubic direction. The relaxed structure is given by the lattice parameters $a = 5.496$ Å and $\alpha = 60.15^\circ$, with atoms located at Fe(0, 0, 0), Bi(0.269, 0.269, 0.269), and O(0.310, 0.168, 0.715). We found an electronic band gap of $E_g = 0.75$ eV. The magnetic moment of the iron atoms $\mu_{\text{Fe}} = 3.572\mu_B$ is in close agreement with previous local-density approximation calculations [41] and experimental data [42].

The zone-center optical phonon modes of the $R3c$ phase can be classified according to the irreducible representations of the C_{3v} point group as

$$\Gamma_{\text{opt}} = 4A_1 \oplus 5A_2 \oplus 9E.$$

The A_1 modes polarized along z and the doubly degenerate E modes polarized in the x - y plane are both Raman and IR active. The computed frequencies are reported in Table IV. The A_2 modes are silent and their frequencies are calculated to be 109, 261, 309, 446, and 577 cm^{-1} .

For these Cartesian axes, the Raman tensors of A_1 and E modes are given by [43]

$$A_1(z) = \begin{pmatrix} a & 0 & 0 \\ 0 & a & 0 \\ 0 & 0 & b \end{pmatrix}, \quad E(x) = \begin{pmatrix} c & 0 & d \\ 0 & -c & 0 \\ d & 0 & 0 \end{pmatrix},$$

$$E(y) = \begin{pmatrix} 0 & -c & 0 \\ -c & 0 & d \\ 0 & d & 0 \end{pmatrix}.$$

The calculated infrared oscillator strengths and Raman tensor elements of the A_1 and E modes are reported in Table IV. The results are in close agreement with those previously reported

TABLE IV. Calculated infrared oscillator strength tensor \tilde{S} ($\times 10^{-4}$ a.u., 1 a.u. = $253.263\,841\,3\text{ m}^3\text{ s}^{-2}$) and Raman tensor elements ($\times 10^{-4}$ bohr $^{3/2}$) of BFO in the $R3c$ phase. Frequencies ω_m are in cm^{-1} .

Modes	ω_m	S_{xx} (S_{zz})	c or a	d or b
$E(\text{TO1})$	102	0.24	39.80	-27.11
$E(\text{TO2})$	152	4.51	70.83	-35.24
$A_1(\text{TO1})$	167	(1.92)	-67.86	-38.26
$A_1(\text{LO1})$	180		76.25	-24.13
$E(\text{TO3})$	237	0.14	-4.78	-182.65
$E(\text{TO4})$	263	1.76	-82.60	-46.09
$A_1(\text{TO2})$	266	(3.51)	10.42	-26.71
$A_1(\text{LO2})$	278		-11.53	-129.53
$E(\text{TO5})$	275	15.73	48.30	-336.00
$A_1(\text{TO3})$	320	(11.03)	-60.77	-406.16
$A_1(\text{LO3})$	427		163.64	339.25
$E(\text{TO6})$	335	0.59	41.66	108.84
$E(\text{TO7})$	378	0.02	-198.47	51.13
$E(\text{TO8})$	408	1.27	-22.73	79.67
$E(\text{TO9})$	509	3.41	-155.51	-62.72
$A_1(\text{TO4})$	517	(1.44)	68.53	322.63
$A_1(\text{LO4})$	533		-167.31	-461.95

in Ref. [26] (using slightly different computational parameters and a finite-difference approach to compute the derivative of the linear optical susceptibilities with respect to atomic displacements). In Table IV we also report the Raman tensor elements of the $A_1(\text{LO})$ modes, highlighting some significant differences from the $A_1(\text{TO})$ modes.

The second-order nonlinear optical susceptibility tensor $\tilde{d} = \frac{1}{2}\tilde{\chi}^{(2)}$ has three independent elements within Kleinman's symmetry ($d_{31} = d_{15}$):

$$d_{ij} = \begin{pmatrix} d_{11} & -d_{11} & 0 & 0 & d_{15} & 0 \\ 0 & 0 & 0 & d_{15} & 0 & -d_{11} \\ d_{15} & d_{15} & d_{33} & 0 & 0 & 0 \end{pmatrix}, \quad (\text{A1})$$

where the indices i and j denote the Cartesian components in Voigt notation. The EO tensor has four independent elements (using Voigt notation for i):

$$r_{i\gamma} = \begin{pmatrix} r_{11} & 0 & r_{13} \\ -r_{11} & 0 & r_{13} \\ 0 & 0 & r_{33} \\ 0 & r_{51} & 0 \\ r_{51} & 0 & 0 \\ 0 & -r_{11} & 0 \end{pmatrix}. \quad (\text{A2})$$

Results with and without scissors correction are reported for the nonlinear optical susceptibilities in Table II and for the electro-optic coefficients in Table III (including the individual electronic and phonon-mediated contributions).

2. The Cm phase

Calculations were performed in the primitive ten-atom Cm phase with C -type AFM structure. The relaxed lattice parameters and atomic positions are summarized in Table V. The matrix defining the three lattice vectors (\mathbf{a} , \mathbf{b} , \mathbf{c}) of this

TABLE V. Relaxed structure of the primitive ten-atom Cm unit cell.

Lattice parameters			
a, b, c (bohrs)	11.231	11.231	7.049
α, β, γ (deg)	91.62	88.38	104.15
Atoms			
	x	y	z
Bi	0.499	0.501	0.972
Bi	0.999	0.001	0.972
Fe	0.530	0.970	0.514
Fe	0.030	0.470	0.514
O	0.346	0.654	0.520
O	0.846	0.154	0.520
O	0.335	0.165	0.553
O	0.600	0.900	0.016
O	0.835	0.665	0.553
O	0.100	0.400	0.016

unit cell is given by (in bohrs)

$$R = \begin{pmatrix} 8.858\,060\,1 & 6.903\,037\,5 & -0.104\,847\,7 \\ -8.858\,060\,1 & 6.903\,037\,5 & 0.104\,847\,7 \\ 0.335\,681\,5 & 0.000\,000\,0 & 7.040\,996\,1 \end{pmatrix}, \quad (\text{A3})$$

where the lattice vectors are in Cartesian coordinates and written by line. We found an electronic band gap of $E_g = 0.56$ eV and the magnetic moment on the iron atoms is $\mu_{\text{Fe}} = 3.679\mu_B$. These values are consistent with previous generalized gradient approximation calculations [36].

 TABLE VI. Calculated infrared oscillator strength tensor \tilde{S} ($\times 10^{-4}$ a.u. with 1 a.u. = $253.263\,841\,3$ m³ s⁻²) and Raman tensor elements ($\times 10^{-4}$) of the TO modes in the Cm phase of BiFeO₃. Frequencies ω_m are in cm⁻¹.

Modes	ω_m	S_{xx} (a or e)	S_{yy} (b or f)	S_{zz} (c)	S_{xz} (d)
A' (TO1)	42	0.00 (0.01)	0.00 (-0.00)	0.00 (0.02)	0.00 (-0.02)
A' (TO2)	65	0.00 (0.00)	0.00 (0.03)	0.00 (0.01)	0.00 (0.00)
A'' (TO1)	84	0.00 (-77.70)	5.88 (-5.70)		
A'' (TO2)	101	0.00 (-0.02)	0.00 (-0.01)		
A' (TO3)	102	0.00 (-0.02)	0.00 (0.01)	0.00 (-0.02)	0.00 (0.01)
A' (TO4)	109	0.47(5.91)	0.00 (275.62)	0.53 (-15.56)	-1.57 (-48.00)
A'' (TO3)	162	0.00 (0.00)	0.00 (0.01)		
A'' (TO4)	188	0.00 (0.00)	0.00 (0.00)		
A' (TO5)	194	0.00 (-20.60)	0.00 (-171.15)	4.52 (-29.86)	-0.38 (138.25)
A' (TO6)	211	1.06 (-14.42)	0.00 (317.36)	1.77 (26.71)	-1.37 (-37.02)
A'' (TO5)	221	0.00 (112.34)	2.79 (17.39)		
A'' (TO6)	234	0.00 (0.10)	0.00 (0.01)		
A' (TO7)	275	0.00 (42.72)	0.00(-625.92)	2.89 (146.71)	-0.10 (21.65)
A' (TO8)	308	0.00 (0.00)	0.00 (0.02)	0.00 (-0.01)	0.00 (0.00)
A'' (TO7)	330	0.00 (-0.02)	0.00 (0.00)		
A' (TO9)	350	1.24 (198.65)	0.00 (267.39)	3.84 (252.16)	-2.18 (-5.27)
A'' (TO8)	359	0.00 (-49.90)	8.42 (-50.79)		
A' (TO10)	369	0.00 (0.08)	0.00 (0.38)	0.00 (0.07)	0.00(0.04)
A' (TO11)	381	9.02(292.31)	0.00 (1507.11)	1.91 (291.70)	4.15 (66.76)
A' (TO12)	421	0.00 (0.01)	0.00 (-0.01)	0.00 (0.01)	0.00 (-0.02)
A' (TO13)	454	0.00 (-0.02)	0.00 (-0.06)	0.00 (-0.04)	0.00 (0.01)
A'' (TO9)	523	0.00 (-0.01)	0.00 (-0.03)		
A'' (TO10)	549	0.00 (-0.04)	0.00 (0.01)		
A' (TO14)	555	1.14 (124.80)	0.00 (469.53)	2.39 (183.53)	-1.65 (-241.44)
A'' (TO11)	600	0.00 (-176.06)	0.90 (-49.65)		
A'' (TO12)	608	0.00 (0.04)	0.00 (0.02)		
A' (TO15)	609	4.08 (-101.40)	0.00 (-422.72)	0.00 (-59.16)	-0.29 (-23.41)

The zone-center optical phonon modes of the Cm phase can be classified according to the irreducible representations of the C_s point group as

$$\Gamma_{\text{opt}} = 15A' \oplus 12A''.$$

Both modes are infrared and Raman active. Here the A'' modes are polarized along the monoclinic axis, while the A' modes are polarized perpendicular to this axis. In this Cartesian system, the Raman tensors are given by [43]

$$A'(x,z) = \begin{pmatrix} a & 0 & d \\ 0 & b & 0 \\ d & 0 & c \end{pmatrix}, \quad A''(y) = \begin{pmatrix} 0 & e & 0 \\ e & 0 & f \\ 0 & f & 0 \end{pmatrix}. \quad (\text{A4})$$

Calculated transverse-optical frequencies, infrared oscillator strengths, and Raman tensor elements of the A' and A'' modes are reported in Table VI.

The d tensor has six independent elements within Kleinman's symmetry ($d_{15} = d_{31}$, $d_{26} = d_{12}$, $d_{32} = d_{24}$, and $d_{35} = d_{13}$) and it can be written as

$$d_{ij} = \begin{pmatrix} d_{11} & d_{12} & d_{13} & 0 & d_{15} & 0 \\ 0 & 0 & 0 & d_{24} & 0 & d_{12} \\ d_{15} & d_{24} & d_{33} & 0 & d_{13} & 0 \end{pmatrix}, \quad (\text{A5})$$

where the indices i and j denote the Cartesian components in Voigt notation. The electro-optic tensor has ten independent

TABLE VII. Calculated independent elements of the nonlinear optical susceptibility (in pm/V) and electronic dielectric tensor of the C_m phase of BiFeO₃ obtained within the LSDA and with an additional scissors correction of 1.75 eV (LSDA + SCI).

Parameter	LSDA	LSDA + SCI
d_{11}	-122.98	-25.21
d_{12}	184.65	39.30
d_{13}	-17.45	7.04
d_{15}	-34.68	-4.08
d_{24}	-114.03	-14.27
d_{33}	-81.38	-11.19
ϵ_{11}^{∞}	8.97	6.36
ϵ_{22}^{∞}	12.87	8.37
ϵ_{33}^{∞}	9.40	6.61
ϵ_{13}^{∞}	-0.77	-0.44

elements given by (using Voigt notation for i)

$$r_{i\gamma} = \begin{pmatrix} r_{11} & 0 & r_{13} \\ r_{21} & 0 & r_{23} \\ r_{31} & 0 & r_{33} \\ 0 & r_{42} & 0 \\ r_{51} & 0 & r_{53} \\ 0 & r_{62} & 0 \end{pmatrix}. \quad (\text{A6})$$

The A' modes couple to r_{11} , r_{21} , r_{31} , r_{51} , r_{13} , r_{23} , r_{33} , and r_{53} , while the A'' modes are linked to r_{42} and r_{62} . Calculations of the second-order nonlinear optical susceptibility (Table VII) and electro-optic responses (Table VIII) were carried out with a scissors correction fixed to 1.75 eV to adjust the calculated electronic band gap to the experimental value of 2.3 eV [44].

This ten-atom primitive unit cell (I) is connected to the 40-atom unit cell (II), which is obtained by doubling the five-atom cell of the ideal perovskite structure along the three Cartesian directions, according to $\mathbf{a}_{\text{II}} = \mathbf{a}_{\text{I}} + \mathbf{b}_{\text{I}}$, $\mathbf{b}_{\text{II}} = 2\mathbf{c}_{\text{I}}$, and $\mathbf{c}_{\text{II}} = \mathbf{a}_{\text{I}} - \mathbf{b}_{\text{I}}$. In this case, we found the following lattice parameters of the quasiperovskite structure: $a_{\text{II}} = 7.306 \text{ \AA}$, $b_{\text{II}} = 7.460 \text{ \AA}$, $c_{\text{II}} = 9.376 \text{ \AA}$, $\alpha = 87.95^\circ$, $\beta = 90^\circ$, and $\gamma = 90^\circ$. These values are in excellent agreement with those obtained by Diéguez *et al.* [36]. Our Cartesian directions were chosen such that the monoclinic \mathbf{a}_{II} axis is along y , the \mathbf{b}_{II} axis is nearly aligned along x , and the \mathbf{c}_{II} axis is nearly aligned along z .

The tensors in this new system of coordinates (II) are provided in the main text. For the third-rank tensors, the change of coordinates from I to II was performed using the following transformation:

$$X_{ijk}^{\text{II}} = \sum_{l,m,n} P_{il} P_{jm} P_{kn} X_{lmn}^{\text{I}}, \quad (\text{A7})$$

where X is the second-order nonlinear susceptibility or the electro-optic tensor and P is the orthogonal passage matrix given by

$$P = \begin{pmatrix} 0 & 1 & 0 \\ \frac{\sqrt{2}}{2} & 0 & \frac{\sqrt{2}}{2} \\ \frac{\sqrt{2}}{2} & 0 & -\frac{\sqrt{2}}{2} \end{pmatrix}. \quad (\text{A8})$$

TABLE VIII. Calculated electronic and ionic contributions to the electro-optic tensor (in pm/V) of the C_m phase of BiFeO₃. The ionic part is split into individual contributions of distinct TO modes. Frequencies ω_m are in cm^{-1} . Our results make use of scissors correction (1.75 eV) for the refractive indices and nonlinear optical susceptibilities (LSDA + SCI values in Table VII). Values without the scissors correction are also reported in parentheses for comparison.

Calculated contribution	A' modes										A'' modes	
	ω_m	r_{11}	r_{21}	r_{31}	r_{51}	r_{13}	r_{23}	r_{33}	r_{53}	ω_m	r_{42}	r_{62}
electronic		(6.50) 2.57	(-4.46) -2.24	(1.12) -0.59	(2.260) 0.52	(1.92) 0.32	(2.75) 0.82	(3.89) 0.95	(1.31) -0.58		(3.27) 0.84	(-6.12) -2.89
ionic	TO4	(0.06) 0.03	(-3.86) -9.14	(0.41) 0.83	(1.38) 2.74	(-0.21) -0.11	(13.05) 30.87	(-1.40) -2.80	(-4.67) -9.26	84	(-0.65) -1.41	(-9.40) -20.30
	TO5	(0.01) -0.01	(-0.20) -0.47	(-0.07) -0.14	(0.32) 0.63	(-0.05) 0.13	(2.35) 5.56	(0.79) 1.59	(-3.73) -7.46	221	(-0.20) -0.43	(-1.36) -2.93
	TO6	(0.24) 0.45	(-1.78) -4.21	(-0.29) -0.58	(0.39) 0.79	(-0.31) -0.58	(2.30) 5.45	(0.37) 0.75	(-0.51) -1.03	359	(-0.38) -0.83	(-0.43) -0.91
	TO7	(0.02) 0.04	(-0.12) -0.28	(0.05) 0.11	(0.01) 0.02	(-0.54) -1.04	(3.40) 8.05	(-1.52) -3.05	(-0.37) -0.68	599	(-0.06) -0.13	(-0.23) -0.49
	TO9	(-0.92) -1.81	(-0.59) -1.39	(-1.06) -2.13	(-0.07) -0.10	(1.62) 3.19	(1.04) 2.46	(1.86) 3.75	(0.12) 0.17			
	TO11	(-3.20) -6.26	(-7.55) -17.86	(-2.78) -5.60	(-0.91) -1.71	(-1.47) -2.88	(-3.47) -8.21	(-1.28) -2.57	(-0.42) -0.79			
	TO14	(-0.15) -0.32	(-0.39) -0.93	(-0.29) -0.59	(0.38) 0.77	(0.22) 0.47	(0.57) 1.35	(0.43) 0.86	(-0.55) -1.11			
	TO15	(-0.29) -0.57	(-0.56) -1.32	(-0.15) -0.30	(-0.07) -0.14	(0.02) 0.04	(0.04) 0.09	(0.01) 0.02	(0.01) 0.00			
sum of ionic		(-4.23) -8.46	(-15.05) -35.61	(-4.17) -8.39	(1.44) 3.00	(-0.72) -0.78	(19.28) 45.62	(-0.74) -1.46	(-10.12) -20.14		(-1.29) -2.79	(-11.40) -24.62
total		(2.26) -5.90	(-19.51) -37.85	(-3.05) -8.97	(3.69) 3.51	(1.21) -0.46	(22.03) 46.43	(3.15) -0.51	(-8.81) -20.71		(1.98) -1.96	(-17.52) -27.52

- [1] G. Catalan and J. F. Scott, *Adv. Mater.* **21**, 2463 (2009).
- [2] S.-W. Cheong and M. Mostovoy, *Nat. Mater.* **6**, 13 (2007).
- [3] M. Bibes, *Nat. Mater.* **11**, 354 (2012).
- [4] M. Bibes and A. Barthélémy, *Nat. Mater.* **7**, 425 (2008).
- [5] J. Allibe, S. Fusil, K. Bouzehouane, C. Daumont, D. Sando, E. Jacquet, C. Deranlot, M. Bibes, and A. Barthélémy, *Nano Lett.* **12**, 1141 (2012).
- [6] D. Lebeugle, D. Colson, A. Forget, M. Viret, P. Bonville, J. F. Marucco, and S. Fusil, *Phys. Rev. B* **76**, 024116 (2007).
- [7] D. Sando *et al.*, *Nat. Mater.* **12**, 641 (2013).
- [8] P. Rovillain, R. de Sousa, Y. Gallais, A. Sacuto, M. A. Méasson, D. Colson, A. Forget, M. Bibes, A. Barthélémy, and M. Cazayous, *Nat. Mater.* **9**, 975 (2010).
- [9] J.-P. Rivera and H. Schmid, *Ferroelectrics* **204**, 23 (1997).
- [10] A. Kumar, R. C. Rai, N. J. Podraza, S. Denev, M. Ramirez, Y.-H. Chu, L. W. Martin, J. Ihlefeld, T. Heeg, J. Schubert, D. G. Schlom, J. Orenstein, R. Ramesh, R. W. Collins, J. L. Musfeldt, and V. Gopalan, *Appl. Phys. Lett.* **92**, 121915 (2008).
- [11] B. Wessels, *Annu. Rev. Mater. Res.* **37**, 659 (2007).
- [12] J. Allibe, K. Bougot-Robin, E. Jacquet, I. C. Infante, S. Fusil, C. Carrétéro, J.-L. Reverchon, B. Marcilhac, D. Creté, J.-C. Mage, A. Barthélémy, and M. Bibes, *Appl. Phys. Lett.* **96**, 182902 (2010).
- [13] J. F. Ihlefeld, N. J. Podraza, Z. K. Liu, R. C. Rai, X. Xu, T. Heeg, Y. B. Chen, J. Li, R. W. Collins, J. L. Musfeldt, X. Q. Pan, J. Schubert, R. Ramesh, and D. G. Schlom, *Appl. Phys. Lett.* **92**, 142908 (2008).
- [14] C. C. Teng and H. T. Man, *Appl. Phys. Lett.* **56**, 1734 (1990).
- [15] J. S. Schildkraut, *Appl. Opt.* **29**, 2839 (1990).
- [16] K. Clays and J. S. Schildkraut, *J. Opt. Soc. Am. B* **9**, 2274 (1992).
- [17] H. Béa, M. Bibes, A. Barthélémy, K. Bouzehouane, E. Jacquet, A. Khodan, J.-P. Contour, S. Fusil, F. Wyczisk, A. Forget, D. Lebeugle, D. Colson, and M. Viret, *Appl. Phys. Lett.* **87**, 072508 (2005).
- [18] X. H. Zhu, H. Béa, M. Bibes, S. Fusil, K. Bouzehouane, E. Jacquet, A. Barthélémy, D. Lebeugle, M. Viret, and D. Colson, *Appl. Phys. Lett.* **93**, 082902 (2008).
- [19] G. E. Jellison, Jr. and J. S. Baba, *J. Opt. Soc. Am. A* **23**, 468 (2006).
- [20] S. H. Wemple and D. DiDomenico, *Applied Solid State Science* (Academic, New York, 1972).
- [21] A. Rauber, in *Current Topics in Materials Science*, Vol. 1 (North-Holland, Amsterdam, 1978), p. 481.
- [22] The Tauc-Lorentz oscillators had the following values: TL₁: $E_0 = 3.346 \pm 0.036$ eV, $\Gamma = 1.15 \pm 0.09$ eV, $A = 4.47 \pm 0.77$ eV; TL₂: $E_0 = 0.11 \pm 0.02$ eV, $\Gamma = 0.463 \pm 0.024$ eV, $A = 84.2 \pm 19.9$ eV; TL₃: $E_0 = 4.59 \pm 0.09$ eV, $\Gamma = 1.96 \pm 0.47$ eV, $A = 6.49 \pm 1.65$ eV; TL₄: $E_0 = 1.35 \pm 0.04$ eV, $\Gamma = 2.28 \pm 0.14$ eV, $A = 6.97 \pm 0.69$ eV; $E_g = 0.0$ eV; $\epsilon_\infty = 3.04 \pm 0.16$; the error was $\chi^2 = 0.3348$.
- [23] P. Yeh, *Optical Waves in Layered Media* (Wiley, Toronto, 1988).
- [24] P. B. Johnson and R. W. Christy, *Phys. Rev. B* **6**, 4370 (1972).
- [25] D. H. Park, C. H. Lee, and W. N. Herman, *Opt. Express* **14**, 8866 (2006).
- [26] P. Hermet, M. Goffinet, J. Kreisel, and Ph. Ghosez, *Phys. Rev. B* **75**, 220102(R) (2007).
- [27] X. Gonze *et al.*, *Comput. Phys. Commun.* **180**, 2582 (2009).
- [28] A. M. Rappe, K. M. Rabe, E. Kaxiras, and J. D. Joannopoulos, *Phys. Rev. B* **41**, 1227 (1990).
- [29] X. Gonze and C. Lee, *Phys. Rev. B* **55**, 10355 (1997).
- [30] M. Veithen, X. Gonze, and Ph. Ghosez, *Phys. Rev. B* **71**, 125107 (2005).
- [31] M. Veithen, X. Gonze, and Ph. Ghosez, *Phys. Rev. Lett.* **93**, 187401 (2004).
- [32] M. Veithen and Ph. Ghosez, *Phys. Rev. B* **71**, 132101 (2005).
- [33] S. Ju, T.-Y. Cai, and G.-Y. Guo, *J. Chem. Phys.* **130**, 214708 (2009).
- [34] J. Hlinka, J. Pokorny, S. Karimi, and I. M. Reaney, *Phys. Rev. B* **83**, 020101(R) (2011).
- [35] C. Beekman, A. A. Reijnders, Y. S. Oh, S. W. Cheong, and K. S. Burch, *Phys. Rev. B* **86**, 020403(R) (2012).
- [36] O. Diéguez, O. E. González-Vázquez, J. C. Wojdeł, and J. Íñiguez, *Phys. Rev. B* **83**, 094105 (2011).
- [37] H. Béa *et al.*, *Phys. Rev. Lett.* **102**, 217603 (2009).
- [38] B. Dupé, I. C. Infante, G. Geneste, P.-E. Janolin, M. Bibes, A. Barthélémy, S. Lisenkov, L. Bellaiche, S. Ravy, and B. Dkhil, *Phys. Rev. B* **81**, 144128 (2010).
- [39] I. C. Infante, J. Juraszek, S. Fusil, B. Dupé, P. Gemeiner, O. Diéguez, F. Pailloux, S. Jouen, E. Jacquet, G. Geneste, J. Pacaud, J. Íñiguez, L. Bellaiche, A. Barthélémy, B. Dkhil, and M. Bibes, *Phys. Rev. Lett.* **107**, 237601 (2011).
- [40] K.-T. Ko, M. H. Jung, Q. He, J. H. Lee, C. S. Woo, K. Chu, J. Seidel, B.-G. Jeon, Y. S. Oh, K. H. Kim, W.-I. Liang, H.-J. Chen, Y.-H. Chu, Y. H. Jeong, R. Ramesh, J.-H. Park, and C.-H. Yang, *Nat. Commun.* **2**, 567 (2011).
- [41] J. B. Neaton, C. Ederer, U. V. Waghmare, N. A. Spaldin, and K. M. Rabe, *Phys. Rev. B* **71**, 014113 (2005).
- [42] F. Kubel and H. Schmid, *Acta Crystallogr. B* **46**, 698 (1990).
- [43] R. Loudon, *Adv. Phys.* **50**, 813 (2001).
- [44] P. Chen, N. J. Podraza, X. S. Xu, A. Melville, E. Vlahos, V. Gopalan, R. Ramesh, D. G. Schlom, and J. L. Musfeldt, *Appl. Phys. Lett.* **96**, 131907 (2010).